

Exfoliated 2D Antimonene-Based Structures for Light-Harvesting Photoactive Layer of Highly Stable Solar Cells

Author

Bat-Erdene, Munkhjargal, Myagmarsereejid, Purevlkham, Bati, Abdulaziz SR, Qin, Jiadong, Zhong, Yu Lin, Shapter, Joseph G, Batmunkh, Munkhbayar

Published

2022

Journal Title

Small Structures

Version

Version of Record (VoR)

DOI

[10.1002/sstr.202200038](https://doi.org/10.1002/sstr.202200038)

Rights statement

© 2022 The Authors. Small Structures published by Wiley-VCH GmbH. This is an open access article under the terms of the Creative Commons Attribution License, which permits use, distribution and reproduction in any medium, provided the original work is properly cited.

Downloaded from

<http://hdl.handle.net/10072/419152>

Funder(s)

ARC

Grant identifier(s)

DE220100521

Griffith Research Online

<https://research-repository.griffith.edu.au>

Exfoliated 2D Antimonene-Based Structures for Light-Harvesting Photoactive Layer of Highly Stable Solar Cells

Munkhjargal Bat-Erdene, Purevlkham Myagmarsereejid, Abdulaziz S. R. Bati, Jiadong Qin, Yu Lin Zhong, Joseph G. Shapter,* and Munkhbayar Batmunkh*

2D materials have shown great promise in various applications including solar cells, but their use as light-harvesting active layers in photovoltaic (PV) devices is limited. Herein, surface-oxidized antimonene sheets are prepared using a liquid-phase exfoliation method and employed as an active light absorber material after functionalization. It is shown that 2D antimonene possesses unique surface chemistry that allows it to form photoactive Sb_2S_3 light absorbers for solar cells under ambient conditions. Under the standard PV testing conditions (AM1.5G), devices fabricated with 2D antimonene-based light-harvesting materials deliver a power conversion efficiency (PCE) of up to 4.28%. This novel type of solar cell exhibits outstanding operational stabilities, preserving >90% of the initial PCE after aging for 60 min at a temperature of 85 °C, retaining >95% of the initial efficiency after exposure to continuous light illumination under 1 sun for 180 min, and maintaining its functionality after being underwater for 25 min. This work opens new avenues for research in 2D materials and photovoltaics.

1. Introduction

With atomically thin sheets of carbon structurally arranged like chicken wire, graphene is strong yet flexible and conducts heat and electricity better than metals (e.g., copper).^[1] Since its 2004 discovery,^[2] graphene has become known as a wonder material and caught a spark in both research and industry sectors. The success of graphene has led to the development of a wide spectrum of 2D materials ranging from insulators to semiconductors to metals.^[3–5] Among various types of 2D materials, monoelemental 2D materials such as phosphorene, borophene, germanene, silicene, and antimonene have drawn increasing research attention in many fields due to their fascinating properties and unique structures.^[6,7]

Antimonene—mono/few atomic layer of antimony (Sb) arranged in a buckled honeycomb structure—is an appealing member of the group V analogues of graphene and has gained a great deal of attention over the past few years.^[8,9] Before its successful synthesis experimentally, 2D antimonene had been well studied theoretically, revealing various attractive properties including high thermal conductivity, excellent carrier mobility, and good spintronic properties.^[10–12] Indeed, in 2016, Zamora's group reported, in two separate studies, the experimental synthesis of 2D Sb nanosheets using mechanical isolation^[13] and liquid-phase exfoliation^[14] methods. Due to its attractive properties and unique features, this exciting material has found applications in many areas such as catalysis,^[15] photo-detectors,^[16] batteries,^[17] supercapacitors,^[18] and so on.


First-principles computational work revealed that 2D Sb nanosheets exhibit tunable bandgaps covering a wide range from 0 to 2.28 eV,^[19] making it attractive for solar cells and photodetectors. However, insignificant attention has been paid to the exploration of 2D antimonene in photovoltaic (PV) applications. Due to their tunable bandgaps and high carrier mobilities, antimonene derivatives have so far been used only as interfacial layers and/or additives to the light-harvesting photoactive layers for solar cells.^[20–22] For instance, Wang et al.^[21] prepared large 2D antimonene nanosheets with a smooth surface using a pregrinding and subsequent sonication-based liquid-phase exfoliation method. The authors were able to tune the bandgap of antimonene nanosheets from 0.8 to 1.44 eV and employed them as a hole transporting layer in perovskite solar cells. Other work by Zhang et al.^[20]

M. Bat-Erdene, J. G. Shapter
Australian Institute for Bioengineering and Nanotechnology
The University of Queensland
Brisbane, Queensland 4072, Australia
E-mail: j.shapter@uq.edu.au

P. Myagmarsereejid, M. Batmunkh
Centre for Catalysis and Clean Energy
School of Environment and Science
Griffith University
Gold Coast, Queensland 4222, Australia
E-mail: m.batmunkh@griffith.edu.au

P. Myagmarsereejid, J. Qin, Y. L. Zhong
Queensland Micro- and Nanotechnology Centre
School of Environment and Science
Griffith University
Gold Coast, Queensland 4111, Australia

A. S. R. Bati
Centre for Organic Photonics & Electronics
School of Chemistry and Molecular Biosciences
The University of Queensland
Brisbane, Queensland 4072, Australia

 The ORCID identification number(s) for the author(s) of this article can be found under <https://doi.org/10.1002/ssstr.202200038>.

© 2022 The Authors. Small Structures published by Wiley-VCH GmbH. This is an open access article under the terms of the Creative Commons Attribution License, which permits use, distribution and reproduction in any medium, provided the original work is properly cited.

DOI: 10.1002/ssstr.202200038

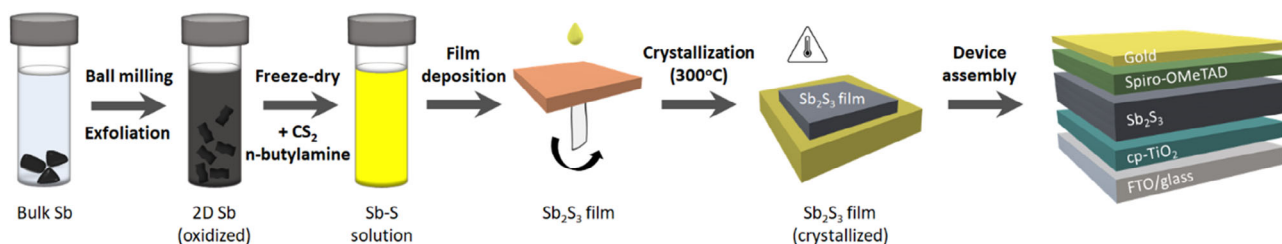


Figure 1. Schematic illustration of the experimental procedures for the sample preparation and device fabrication.

reported the use of monolayer antimonene nanosheets as hole extraction layers in perovskite solar cells and observed some enhancements in the PV efficiencies. Furthermore, Guo and co-workers prepared atomically thin antimonene quantum sheets using imidazolium ionic liquid-assisted exfoliation.^[22] They used their as-prepared antimonene sheets as an additive to the photoactive layer of organic solar cells and observed a noticeable enhancement in the PV performance. These findings indicate the great potential of antimonene in PV applications. However, to the best of our knowledge, no effort has been made in using 2D antimonene derivatives as an active light-harvesting component in solar cells. Recently, our group showed that the 2D layered antimonene sheets as well as the bulk Sb crystals present some surface oxidation, which could be useful for different applications.^[23] In addition, the oxidized species of 2D antimonene sheets can act as excellent reactive sites for further functionalization.

In this work, we report efficient solution-processable solar cells with outstanding operational stabilities based on Sb_2S_3 light absorber photoactive materials prepared from surface-oxidized 2D antimonene (**Figure 1**). First, 2D antimonene sheets with abundant surface oxidation were prepared via a combination of ball milling and sonication-assisted exfoliation, followed by functionalization using sulfur containing chemicals including carbon disulfide (CS_2) to obtain Sb_2S_3 light-harvesting materials. Then the as-prepared Sb_2S_3 solar absorbers were used to fabricate solar cells with an n–i–p-type device architecture. In addition to the PV performances including hysteresis and scan-rate-dependent tests, various operational stabilities (thermal, long-term, and humidity) have been systematically assessed.

2. Results and Discussion

2.1. Preparation and Characterization of Exfoliated 2D Sb Flakes

Figure 1 illustrates the experimental procedures of the sample preparation and device fabrication. Bulk Sb crystal was ground using a mortar and pestle (Figure S1 and S2, Supporting Information) and added into a mixed solvent (isopropanol/water; 4:1) for liquid-phase exfoliation using a combination of ball milling and ultrasonication. The exfoliated Sb sample was examined using various characterization techniques. A broad absorption spectrum with one main peak at 230–250 nm can be observed for our exfoliated Sb dispersion which is consistent with the UV–vis spectra of antimonene reported in previous studies

(Figure S3a, Supporting Information).^[20,23] Antimonene is a layered 2D material consisting of sheets of sp^3 -hybridized antimony atoms with Sb–Sb bonds, but mildly or severely oxidized on its surface, according to recent literature.^[23–25] In order to explore the structural and morphological characteristics of the exfoliated Sb flakes, several spectroscopic and microscopic techniques were employed. It can be seen from **Figure 2a** that the X-ray diffraction (XRD) result of our exfoliated Sb showed a pattern consistent with that of the antimonene reported in the literature.^[25] The XRD pattern exhibits all characteristic peaks of a typical Sb powder. For comparison, XRD characterization was carried out on the commercial Sb_2O_3 powder. As illustrated in Figure S3, Supporting Information, the observed XRD pattern of the Sb_2O_3 was different from the exfoliated Sb, suggesting that the surface oxidation of exfoliated Sb flakes cannot be detected by XRD technique. As XRD cannot provide very precise information on chemical and structural characteristics, Raman spectroscopy was used for the exfoliated Sb sample. As expected, our exfoliated Sb flakes showed two characteristic peaks at 117.0 cm^{-1} (E_g) and 149.2 cm^{-1} (A_{1g}) due to the in-plane and out-of-plane vibrational modes of β -phase antimonene (Figure 2b).^[26] In addition to these two peaks, several Raman modes centered at 190.0, 256.5, 371.1, and 456.1 cm^{-1} were also observed and can be assigned to the oxidized states of antimony (Sb_2O_3).^[26] This suggests that the exfoliated Sb sample is mildly oxidized.

To further study the chemical structure of the exfoliated Sb flakes including their oxidation, X-ray photoelectron spectroscopy (XPS) was used (Figure 2c). The high-resolution XPS spectrum (Sb 3d) of our exfoliated Sb sample is illustrated in Figure 2d and can be deconvoluted into two main spin–orbit split doublets from the metallic and oxide forms of Sb (Sb $3d_{5/2}$ and Sb $3d_{3/2}$), in addition to the O 1s peak. The binding energy difference in the doublet peaks was measured to be 9.40 eV, which is in excellent agreement with the XPS practical guide.^[27] Two small peaks at the binding energies of 528.3 and 537.7 eV are associated with the Sb $3d_{5/2}$ and Sb $3d_{3/2}$ of metallic Sb (Sb^0), while the intense peaks centered at 530.5 and 539.9 eV can be assigned to the oxidized Sb (Sb_2O_3).^[23,28] These XPS features are consistent with our XRD and Raman analysis, suggesting that the exfoliated 2D Sb flakes are strongly oxidized on their surfaces. Such oxidation on the surface of exfoliated 2D Sb flakes are believed to originate from the use of grinding and ball milling steps during the sample preparation.^[29] These oxidized species of exfoliated 2D Sb are expected to act as effective reactive sites for further functionalization. Figure 2e shows the transmission electron microscopy (TEM) image of the exfoliated Sb sample,

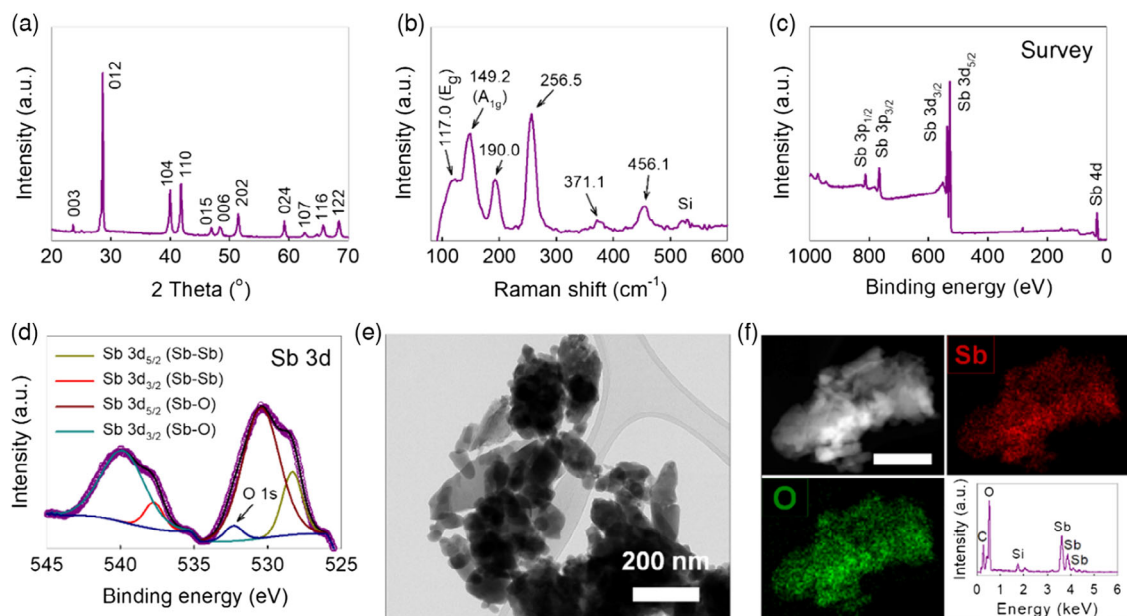


Figure 2. a) XRD pattern, b) Raman spectrum, c) XPS survey scan, d) high-resolution XPS (Sb 3d) spectrum, e) TEM image, and f) HAADF-STEM image, EDX elemental mapping (Sb and O) and EDX spectrum of the exfoliated Sb flakes. Scale bar in (f): 200 nm.

revealing its aggregated 2D morphology with a flake lateral size of around 200–300 nm. High-angle annular dark-field scanning transmission electron microscopy (HAADF-STEM), energy-dispersive X-ray (EDX) elemental mapping images and EDX spectrum of the exfoliated Sb flakes are shown in Figure 2f. The presence of Sb and O elements in both EDX elemental mapping and spectrum further confirms the successful preparation of surface-oxidized Sb flakes. Atomic force microscopy (AFM) was used to confirm the 2D flake structure of our surface-oxidized Sb sample. Figure S4, Supporting Information, shows the representative AFM images of the exfoliated 2D Sb flakes with diameters ranging from a hundred to few hundreds of nanometers, which is consistent with the measured lateral sizes from the TEM images. The thicknesses of the flakes were measured from the height profile data in Figure S4, Supporting Information, and had a distribution ranging from 30 to 60 nm, suggesting multilayer oxidized Sb sheets. These are reasonable values given the Sb sample was not centrifuged prior to use as we aimed to obtain a large quantity of exfoliated Sb flake powder for device fabrication. Notably, the production of single- or few-layer Sb nanosheets was not the aim of this work.

2.2. Preparation and Characterization of Sb_2S_3 Thin Films

The exfoliated Sb sample was then sulfurized to obtain Sb_2S_3 light-harvesting photoactive semiconducting materials by reacting with carbon disulfide (CS_2) and dimethyl sulfoxide (DMSO) in *n*-butylamine. For comparison, commercial Sb_2O_3 powder was also used for the preparation of Sb_2S_3 . The color of the solution with exfoliated Sb flakes was black upon mixing with CS_2 (first day), DMSO, and *n*-butylamine, while the solution prepared from commercial Sb_2O_3 powder was yellow. After stirring for 5 days continuously, both exfoliated Sb flakes and

commercial Sb_2O_3 powder were completely dissolved, and the solutions were clear yellow (Figure S5, Supporting Information) and remained stable for over a month. The as-prepared precursor solutions were deposited on TiO_2 coated fluorine-doped tin oxide (FTO) glass substrates, followed by annealing at 200 °C for 1 min and 300 °C for 2 min in air (Figure S6, Supporting Information). It is well known that due to their high sensitivity to ambient atmosphere, high efficiency PV devices are mainly constructed in an inert environment,^[30,31] raising questions regarding the long-term stability and manufacturing costs of the devices. Therefore, developing high-efficiency and stable solar cells that can be constructed under ambient conditions is very appealing. In addition, a recent theoretical study suggested that oxygen doping (O doping) in Sb_2S_3 is an effective strategy to enhance the PV performance by increasing the p-type conductivity and hole carrier concentration due to the low formation energy of O_{Sb} .^[32] Ambient fabrication of Sb_2S_3 solar cells is expected to introduce O doping in Sb_2S_3 light absorbers.

The UV-vis spectrum of the Sb_2S_3 thin film (cyan color) is plotted in Figure 3a and shows a broad light absorption at wavelengths ranging from 350 to 600 nm. As illustrated in Figure S7, Supporting Information, high-resolution XPS spectra of the Sb_2S_3 thin film fabricated in air showed strong peaks associated with Sb_2S_3 without any oxidized Sb species, revealing that surface-oxidized Sb was successfully sulfurized to form Sb_2S_3 . The fabrication of solar cells was completed by coating a hole transporting material and a metal electrode on top of the Sb_2S_3 films annealed in air. Figure S8, Supporting Information, shows the current density–voltage (*J*–*V*) characteristics of the best performing Sb_2S_3 device fabricated from exfoliated 2D Sb flakes under ambient conditions. The average PV parameters of these solar cells such as short-circuit current

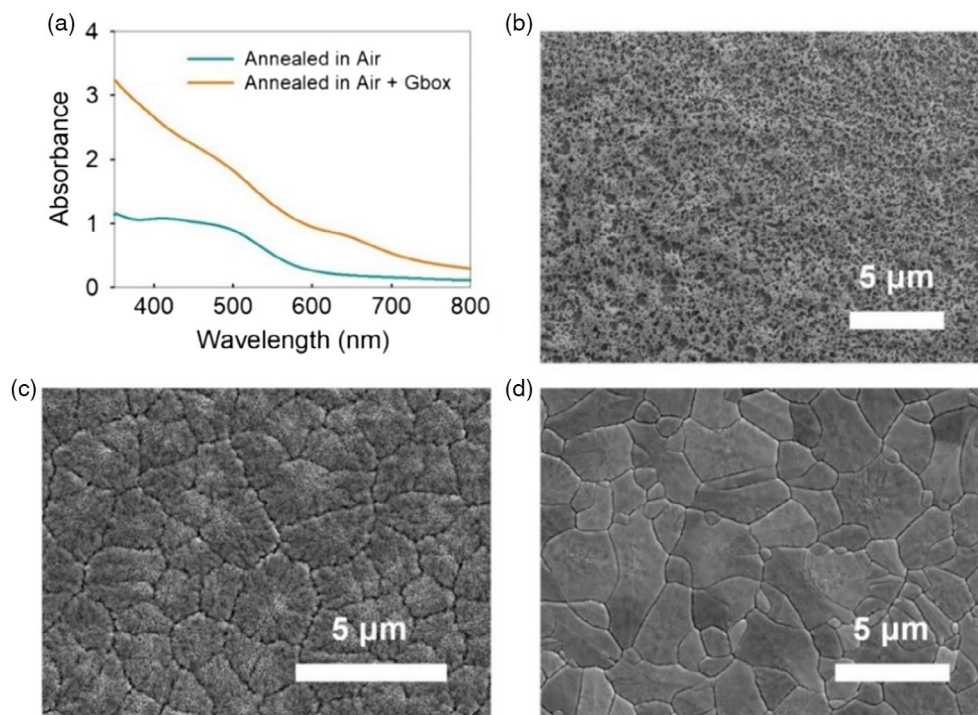


Figure 3. a) UV-vis spectra of Sb_2S_3 thin film fabricated by annealing in air only (cyan color) and in both air and glove box (orange color). SEM image of Sb_2S_3 film prepared by annealing b) in air only (200 °C for 1 min and 300 °C 2 min), c) in both air (200 °C for 1 min and 300 °C 2 min) and glove box (300 °C for 1 min), and d) in both air (200 °C for 1 min and 300 °C 2 min) and glove box (300 °C for 2 min).

(J_{sc}), open-circuit voltage (V_{oc}), fill factor (FF), and power conversion efficiency (PCE) (%) have been summarized in Table S1, Supporting Information. However, the devices fabricated in air suffered from poor PV performance with an average PCE of 1.73%. The best performing device displayed a PCE of only 1.96% with the measured J_{sc} of 14.16 mA cm^{-2} , V_{oc} of 0.46 V, and FF of 0.30 (Figure S8, Supporting Information), which suggest that further steps are required to enhance these PV parameters.

A scanning electron microscopy (SEM) image of the exfoliated 2D Sb flakes-based Sb_2S_3 thin film fabricated in air is shown in Figure 3b. It can be observed that the Sb_2S_3 film annealed only in air exhibits a porous structured morphology without any measurable crystal grain structures, suggesting that annealing Sb_2S_3 in air is ineffective to obtain crystalline light-harvesting photoactive film for solar cells. The air-annealed Sb_2S_3 film was then transferred into an inert gas (argon) filled glove box for further annealing process. Interestingly, after annealing the film for only 1 min, we started to observe some changes in the film morphology. As shown in Figure 3c, large grain sizes with an average size of 1–2 μm can be observed from the Sb_2S_3 thin film fabricated in air followed by annealing in a glove box for 1 min. However, a large number of pinholes in this Sb_2S_3 film suggest that the crystallization of the film was incomplete and poor. Indeed, we were able to obtain highly crystalline Sb_2S_3 thin films without pinholes by annealing the air-annealed Sb_2S_3 films in a glove box for 2 min at 300 °C (Figure 3d). The grain sizes in these completely crystallized Sb_2S_3 films can be measured to be 1–4 μm , which will be beneficial for efficient charge extraction

and transport in solar cells. It should be noted that annealing air-annealed Sb_2S_3 films in a glove box for less than 2 min results in an incomplete crystallization of the film (Figure S9, Supporting Information). For comparison, we also prepared Sb_2S_3 thin films from commercial Sb_2O_3 powder using the same approaches (annealing in air and in glove box). However, the commercial Sb_2O_3 powder-based Sb_2S_3 film suffered from smaller grain sizes and noticeable pinholes (Figure S10, Supporting Information) as compared to the Sb_2S_3 thin film prepared from the exfoliated 2D Sb flakes.

As depicted in Figure 3a, Sb_2S_3 thin films fabricated by annealing in both air and the glove box displays extended light absorption in the UV and visible regions. In addition, the higher absorption intensity of this Sb_2S_3 film, in comparison to the Sb_2S_3 film prepared by annealing only in air, suggests effective light-harvesting properties for solar cells. Figure S11, Supporting Information, shows a photograph of Sb_2S_3 thin films after annealing both air and glove box. We then used XPS to investigate the chemical composition of the Sb_2S_3 thin films. **Figure 4** shows the XPS analysis of the Sb_2S_3 film prepared from the exfoliated 2D Sb flakes (orange, Figure 4a–c) and commercial Sb_2O_3 powder (green, Figure 4d–f). According to the survey spectra (Figure 4a,d), only Sb and S can be observed from both Sb_2S_3 films, revealing the high purity of the samples. The HR Sb 3d spectrum of the Sb_2S_3 thin films showed two strong peaks at around 529.2 and 538.6 eV, which can be assigned to the Sb 3d_{5/2} and Sb 3d_{3/2} of Sb^{3+} (in particular sulfides), respectively.^[27] Furthermore, the S 2p spectrum in Figure 4c exhibited the peaks at binding energies of 161.15 and 162.3 eV, which are associated

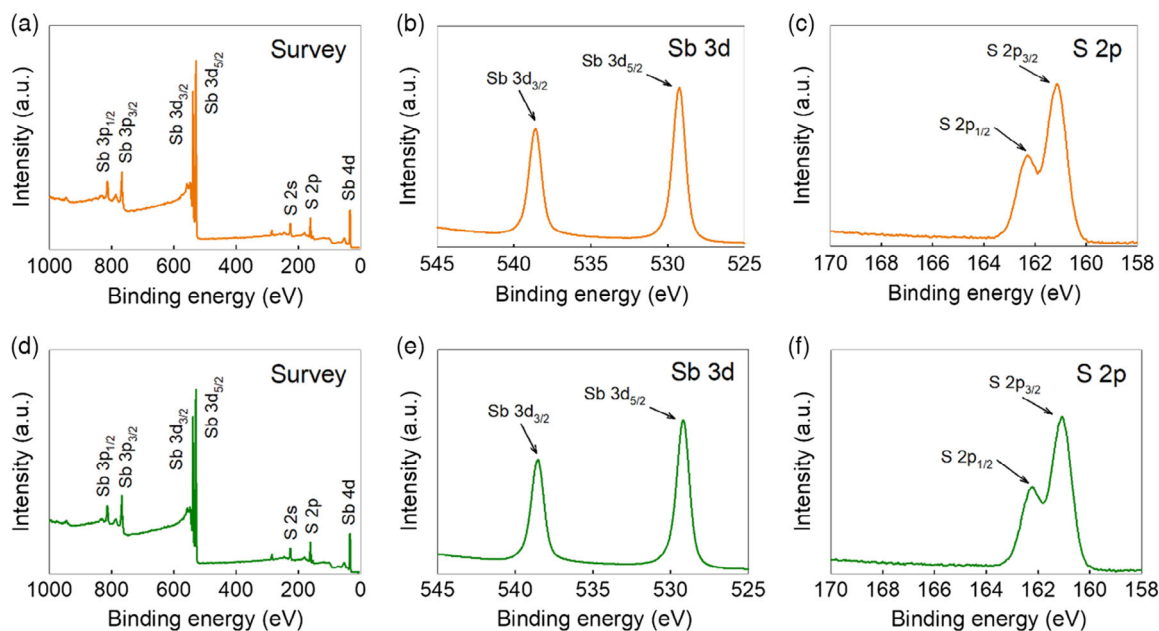


Figure 4. XPS a) survey scan, b) HR Sb 3d spectrum, and c) HR S 2p spectrum of Sb_2S_3 thin film fabricated from the exfoliated 2D Sb flakes by annealing in both air and glove box. XPS d) survey scan, e) HR Sb 3d spectrum, and f) HR S 2p spectrum of commercial Sb_2O_3 powder-based Sb_2S_3 thin film prepared by annealing in both air and glove box.

with $\text{S } 2p_{3/2}$ and $\text{S } 2p_{1/2}$, respectively, suggesting a single doublet with splitting of 1.15 eV from the S–Sb bonds. Importantly, the absence of any peak at binding energies between 165 and 170 eV suggests that the films were stable with no significant oxidation. It should be noted that no differences in the HR Sb 3d and S 2p spectra were observed from both Sb_2S_3 samples, demonstrating that the exfoliated 2D Sb flakes can be used as a precursor material for photoactive Sb_2S_3 films.

2.3. Photovoltaic Performances of Sb_2S_3 Solar Cells

All devices were then fabricated by annealing Sb_2S_3 -coated TiO_2/FTO electrodes in both air and the glove box. **Figure 5a** shows the cross-sectional SEM image of the full device with a layered structure of $\text{FTO}/\text{TiO}_2/\text{Sb}_2\text{S}_3/\text{Spiro-OMeTAD}/\text{Au}$. To optimize the thickness of the light-harvesting layer, Sb_2S_3 solar cells were fabricated by spin coating precursor solutions (prepared from exfoliated 2D Sb flakes) at different speeds ranging from 4000 to 7000 rpm. The PV characteristics of the devices were investigated under an air mass (AM) 1.5 illumination at 100 mW cm^{-2} . **Figure 5b** displays the J – V curves of the Sb_2S_3 solar cells fabricated using different deposition speeds and their corresponding PV parameters (J_{sc} , V_{oc} , FF, and PCE) have been summarized in **Table 1**.

It is well known that the thickness optimization of the light absorber layer is the key to achieving efficient solar cells. A thin photoactive layer offers limited photon absorption resulting in poor J_{sc} values, while a thick layer suffers from significant charge (electron–hole) recombination and adversely affects all PV parameters. In terms of an optimal thickness of Sb_2S_3 photoactive layer, the solar cells fabricated by spin coating Sb_2S_3 solutions at a speed of 6000 rpm showed the highest

PV performance with an average PCE of $3.66 \pm 0.36\%$ (**Table 1**). The measured J_{sc} , V_{oc} , and FF values for the best performing Sb_2S_3 solar cell were 16.66 mA cm^{-2} , 0.59 V, and 0.44, respectively, yielding an efficiency of 4.28%. The measured thickness of the Sb_2S_3 film obtained using 6000 rpm was around 120 nm. It can be observed from **Figure 5b** and **Table 1** that all three PV parameters of the solar cells constructed based on 4000 and 5000 rpm (thicker than 120 nm) were lower than those obtained by the optimized devices (6000 rpm), resulting in lower efficiencies. These poor device performances with thicker Sb_2S_3 films are believed to be due to the high charge trapping and recombination issues within the thicker films.^[33] In particular, such issues associated with the charge recombination might be responsible for the reduced V_{oc} and FF values, which were also observed in previous studies.^[34,35] On the other hand, the solar cells fabricated with thin Sb_2S_3 layers obtained using 7000 rpm delivered dramatically reduced J_{sc} values due to their limitations in absorbing light, and thus exhibiting lower cell efficiencies as compared to the 120 nm Sb_2S_3 thickness-based devices.

For comparison, we also fabricated solar cells using the commercial Sb_2O_3 powder-based Sb_2S_3 precursor solution. However, the observed J_{sc} , V_{oc} , and FF values for the best Sb_2S_3 solar cell fabricated using commercial Sb_2O_3 were 14.19 mA cm^{-2} , 0.56 V, and 0.36, respectively, yielding a PCE of only 2.84% (**Figure S12**, Supporting Information), which is significantly lower than that (4.28%) of the 2D Sb flakes-based Sb_2S_3 solar cells. This suggests that the 2D Sb flakes are promising candidates for developing highly efficient light-harvesting photoactive materials for solar cells. Various deposition strategies using different starting materials have been developed to prepare light-harvesting Sb_2S_3 thin films for solar cells.

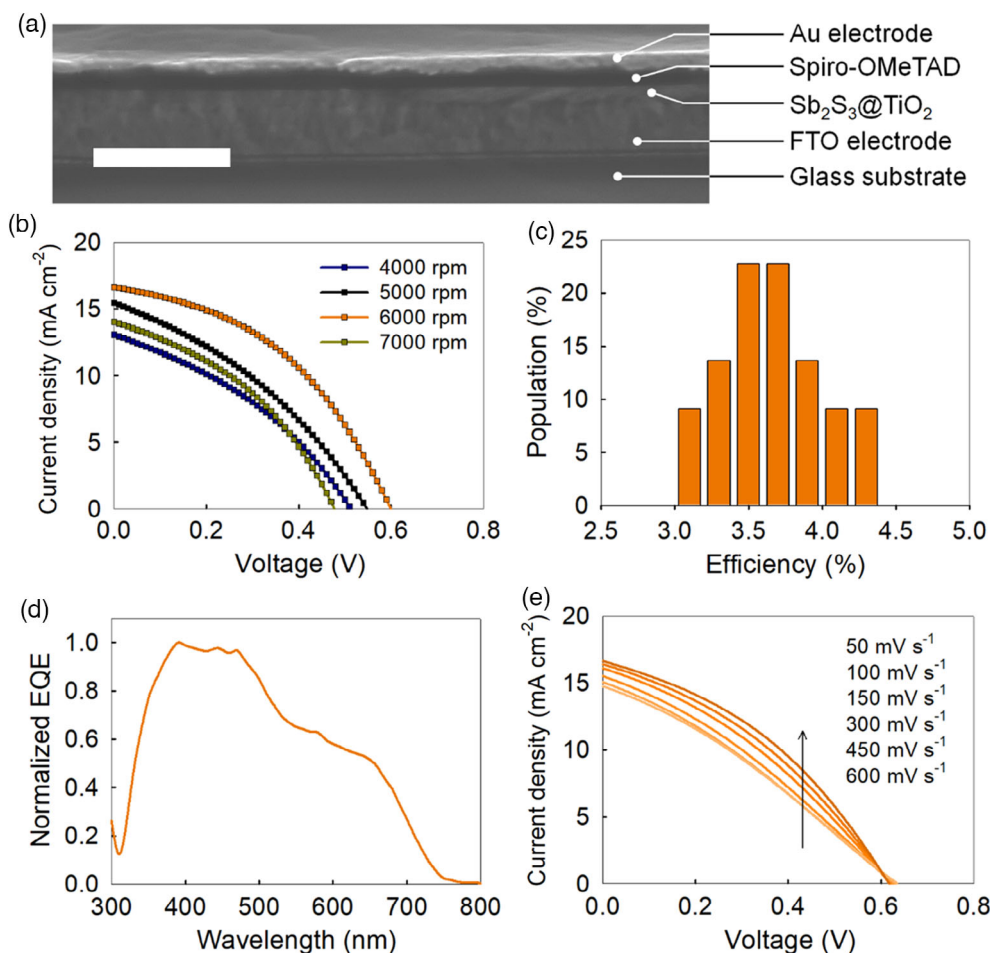


Figure 5. a) Cross-sectional SEM image of a fabricated Sb_2S_3 solar cell based on the exfoliated 2D Sb flakes. Scale bar: 1 μm . b) J - V curves of Sb_2S_3 solar cells fabricated by spin coating Sb_2S_3 precursor solutions using different speeds. The scans were made under reverse (from 0.8 to -0.1 V) direction. c) Efficiency histogram of the fabricated Sb_2S_3 solar cells using 6000 rpm speed of spin coating calculated based on 22 individual cells. d) Normalized EQE spectrum of the best performing Sb_2S_3 solar cell. e) J - V curves of the exfoliated 2D Sb flakes-based Sb_2S_3 solar cell measured at different scan rates.

Table 1. Detailed PV parameters of the solar cells fabricated by spin coating Sb_2S_3 precursor solutions using different speeds. Parameters for the best cells are in bold.

	J_{sc} [mA cm^{-2}]	V_{oc} [V]	FF	PCE [%]
4000 rpm	13.10;	0.51;	0.36;	2.41;
	10.55 ± 2.03	0.48 ± 0.04	0.34 ± 0.02	1.73 ± 0.47
5000 rpm	15.47;	0.54;	0.36;	2.97;
	14.15 ± 1.33	0.55 ± 0.02	0.34 ± 0.02	2.66 ± 0.37
6000 rpm	16.66;	0.59;	0.44;	4.28;
	16.99 ± 0.96	0.57 ± 0.04	0.38 ± 0.03	3.66 ± 0.36
7000 rpm	14.06;	0.47;	0.40;	2.61;
	11.84 ± 2.34	0.46 ± 0.03	0.37 ± 0.02	2.01 ± 0.38

Table S2, Supporting Information, compares the PV parameters of Sb_2S_3 solar cells fabricated using different deposition methods and precursor materials in order to illustrate the effectiveness of our surface-oxidized 2D Sb flakes as a starting material.

Dark J - V measurements inject carriers into the circuit with electrical connections rather than the photogenerated carriers and are effective for analyzing the electrical characteristics of solar cells. As such, we carried out dark J - V measurements at forward and reverse bias on our device with 120 nm Sb_2S_3 layer. As shown in Figure S13, Supporting Information, the dark current density (at $V = 0$ V) was measured from the dark J - V curve with a linear scale to be $5.90 \times 10^{-5} \text{ mA cm}^{-2}$. This value is relatively high and may be responsible for the V_{oc} loss of the system.^[36] In addition, a semilog plot of the dark J - V curve, as illustrated in the inset of Figure S13, Supporting Information, provides further information on the fundamental performance parameters. The relatively high current density values measured in the low-voltage region suggest the reduced shunt resistance of the device,^[37] leading to relatively poor FF values observed in our devices.

A histogram showing the PCE of a total of 22 individual devices is displayed in Figure 5c. The histogram clearly suggests that this novel type of solar cells fabricated using 2D Sb flakes are very reproducible. Figure 5d shows the normalized external

quantum efficiency (EQE) spectrum of the best performing Sb_2S_3 solar cell. It can be seen from the EQE spectrum that the device exhibits a broad absorption at wavelengths ranging from 300 to 750 nm, which is consistent with the UV–vis spectrum of the thin film (see Figure 3a). Moreover, as depicted in Figure S14, Supporting Information, compared to the solar cell prepared with commercial Sb_2O_3 powder, the EQE spectrum of our 2D Sb flakes-based device shows wider light absorption from 300 to 450 nm and 625 to 750 nm, demonstrating its excellent absorption properties. It is well documented that the J – V curves of emerging solar cells are heavily dependent on both scan rate and direction.^[38,39] Therefore, it is important to explore the effect of scan rate and direction on the PV characteristics of novel types of solar cells. For instance, it is well known that perovskite solar cells show an obvious increase in the PCEs when increasing the scan rates caused mainly by the changes in the measured J_{sc} values.^[38,40] Figure 5e depicts the J – V curves of Sb_2S_3 solar cells fabricated using 2D Sb flakes measured at various scan rates (50–600 mV s^{-1}). Unlike perovskite solar cells, the J_{sc} values of our Sb_2S_3 solar cells decreased when increasing the scan rates, while V_{oc} and FF values remained unchanged. This change in the J_{sc} resulted in a nearly 25% difference in the PCEs when the scan rate was changed from 50 to 600 mV s^{-1} . For comparison, we also carried out J – V scans on the Sb_2S_3 solar cells fabricated using commercial Sb_2O_3 powder at different rates (50–600 mV s^{-1}). Interestingly, almost no change was observed in all PV parameters with a slight exception of V_{oc} values of commercial Sb_2O_3 -based solar cells (Figure S15, Supporting Information). This interesting phenomenon should be carefully investigated in the future studies of Sb_2S_3 solar cells.

2.4. Robustness and Stability of Sb_2S_3 Solar Cells

Widespread commercialization of solar technologies will only be possible if the issues associated with the stability and reliability of novel types of solar cells are solved.^[41] As such, testing operational stabilities of solar cells under various conditions is the key to the development of the new technologies. One of the critical tests for solar cells is the examination of the hysteresis effect observed in the J – V curves when scanning in reverse and forward directions.^[40,42] Figure 6a illustrates the J – V curves of our Sb_2S_3 solar cells fabricated from 2D Sb flakes measured using reverse (from 0.8 to -0.1 V) and forward (from -0.1 to 0.8 V) directions. In general, noticeable changes in the FF values have been observed in emerging PV devices such as perovskite solar cells from the J – V measurements under reverse and forward directions.^[38] Interestingly, while no changes were seen in the V_{oc} and FF values, we observed a considerable increase in the J_{sc} value of our Sb_2S_3 solar cells (from 16.64 to 18.74 mA cm^{-2}) when changing the scan direction from reverse to forward. This unusual finding opens a new research avenue and should be explored in future studies.

One of the key challenges for solar technologies is their sensitivity to moisture (high humidity). We tested our Sb_2S_3 solar cells after dipping them in water for 0, 1, and 25 min, and the corresponding J – V curves are shown in Figure 6b. After dipping for only 1 min, no significant change in the efficiency of the solar cells was seen. Surprisingly, the cell was able to retain more than 60% of its initial PCE after being underwater for 25 min (degraded from 3.29% to 2.05%), despite no encapsulation or protection on our devices. This is a very promising result

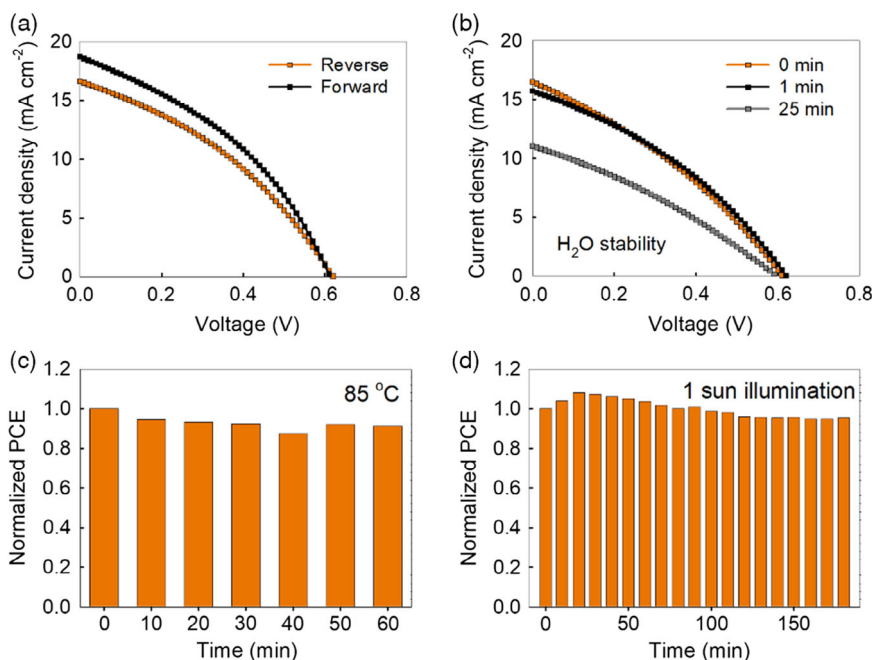


Figure 6. a) J – V curves of the exfoliated 2D Sb flakes-based Sb_2S_3 solar cells measured using reverse (from 0.8 to -0.1 V) and forward (from -0.1 to 0.8 V) scan directions. b) J – V curves of Sb_2S_3 solar cells measured before and after dipping devices in water (H_2O) for 0, 1 and 25 min. Normalized PCE of the devices as a function of time after c) annealing at a temperature of 85 °C and d) continuous light illumination under 1 sun.

demonstrating the excellent operational stability of this class of novel solar cells. This exceptional stability of our Sb_2S_3 solar cells underwater suggests that these novel PV devices open new research directions such as employing them as underwater solar cells. The significant benefits of using PV devices underwater include addressing land use restrictions, protecting cells from thermal degradation and others.^[43,44] The key requirement for underwater solar cells is the excellent device stability and its operation underwater, for which our new type of Sb_2S_3 solar cells show a great promise.

When solar cells are operating under sunlight, a considerable level of heat is applied to the devices.^[45,46] Therefore, we applied a temperature of 85 °C heating (on a hotplate) to our solar cells in ambient conditions and tested every 10 min for a total of 1 h. Figure 6c shows the normalized PCE of the solar cells as a function of heating time (min) at 85 °C temperature. Notably, the initial PCE of 3.44% degraded to 3.14% over 1 h heating at 85 °C, retaining more than 90% of its initial performance. In addition to the moisture and thermal stabilities, the light stability of the solar cells (unencapsulated) was studied by exposing devices to continuous light illumination (100 mW cm⁻², xenon lamp) for 180 min. The data were collected in the reverse scan direction every 10 min in an ambient atmosphere. Figure 6d displays the normalized PCE of the devices as a function of exposure time to continuous light illumination. Promisingly, the device retained more than 95% of its initial PCE after 180 min of irradiation. These operational test results demonstrate that this novel type of solar cells fabricated using 2D Sb flakes not only deliver good efficiencies, more importantly they are able to pass harsh moisture, light exposure, and thermal tests.

3. Conclusion

A novel type of solar cell has been developed using exfoliated 2D Sb flakes-based light-harvesting photoactive layer. Surface-oxidized 2D antimonene exhibits unique surface chemistry, allowing it to form Sb_2S_3 light absorber materials for solar cells. We also found that annealing Sb_2S_3 thin films in both air and a glove box is vital to obtain highly crystalline light-harvesting films with large grain sizes. As a result, a PCE of up to 4.28% has been achieved using 2D Sb flakes-based Sb_2S_3 solar cells when tested under 1.5 global light with an intensity of 100 mW cm⁻² in air. We demonstrated that Sb_2S_3 solar cells with efficiencies ranging from 3% to 4.3% are highly reproducible. More importantly, this new class of solar cells showed outstanding operational stabilities such being able to withstand harsh moisture, light exposure, and thermal tests. Due to their excellent stabilities, our Sb_2S_3 solar cells exhibit a great promise for new solar technologies such as underwater solar cells. Finally, we suggest that future progress on this novel type of solar cells should pay particular attention on enhancing their PV efficiencies, understanding the hysteresis effect and unstable characteristics observed at different scan rates.

4. Experimental Section

Materials and Synthesis: Unless otherwise specified, all chemicals were obtained from Sigma-Aldrich Co., Ltd., Australia. Crystalline antimony (Sb)

(99.9999% purity) was purchased from Smart Elements. A hole transporting material (HTM), 2,2',7,7'-Tetrakis(*N,N*-di-*p*-methoxyphenylamine)-9,9'-spirofluorene (spiro-OMeTAD), was purchased from Xi'an Polymer Light Technology Corp.

Bulk Sb crystals were ground using a mortar and pestle before being added into a 4:1 isopropanol/water mixture, followed by exfoliating using a combination of ball milling and ultrasonication. The ball milling was carried out in a zirconia milling pot at a rotation speed of 300 rpm for 30 min. After drying in an oven, the ball-milled Sb flakes mixed with isopropanol/water mixture (4:1) for further exfoliation using a bath ultrasonication for 1 h. The exfoliated Sb flakes were then freeze-dried to obtain surface-oxidized Sb flake powder.

The preparation of Sb_2S_3 precursor solution was carried out according to the procedure described previously.^[47] Briefly, surface-oxidized Sb flakes or commercial Sb_2O_3 powder (48.50 mg) were added into a glass vial containing 208 μL DMSO (anhydrous, $\geq 99.9\%$), 125 μL ethanol, 250 μL carbon disulfide (anhydrous CS_2 , $\geq 99\%$), and 330 μL *n*-butylamine (99.5%). After 5 days of vigorous magnetic stirring at 300 rpm in a fume hood, the powders were completely dissolved and the precursor solution was obtained.

Device Fabrication: FTO-coated glass substrates (prepatterned) were cleaned by sequentially ultrasonating in a detergent, Milli-Q water, acetone, and isopropanol for 10 min each. Before depositing the electron transporting layer, the FTO substrates were then cleaned using an oxygen plasma (Tergeo Plasma Cleaner) for 10 min. A thin TiO_2 layer (≈ 30 nm) was deposited onto the FTO substrate by spin coating 0.15 M titanium diisopropoxide bis(acetylacetonate) (75 wt% in IPA) in 1-butanol solution at 3000 rpm for 45 s, followed by annealing at 150 °C for 15 min and 500 °C for 1 h. The precursor solutions (Sb_2S_3) were then filtered before being spin-coated onto the electron transporting TiO_2 layers. The spin coating was carried out at 4000–7000 rpm for 30 s in air, followed by annealing at 200 °C and 1 min and 300 °C for 2 min in air (inside fume hood). The Sb_2S_3 deposited films were then transferred into a glove box (argon filled) for the final annealing at 300 °C for 2 min. The fully crystallized Sb_2S_3 films were then posttreated with DMSO solution containing thiourea ($\geq 99.0\%$) (1 M) by spin coating at 5000 rpm for 30 s, followed by annealing 300 °C for 5 min.

The hole transporting layer of Spiro-OMeTAD was spin-coated onto the Sb_2S_3 layers at 3000 rpm for 30 s. A HTM solution was prepared by dissolving 36.6 mg Spiro-OMeTAD, 14.5 μL 4-*tert*-butylpyridine (*t*BP, 98%), and 9.5 μL of a stock solution of 520 mg mL⁻¹ lithium bis(trifluoromethylsulfonyl)imide (Li-TFSI, 99.95%) in acetonitrile, in 1 mL chlorobenzene. The devices were then left inside a desiccator overnight to improve the conductivity of the Spiro-OMeTAD for enhanced charge transport.^[48] Finally, a 80 nm gold electrode was thermally evaporated onto the Spiro-OMeTAD-coated films under a high vacuum at a rate of 0.1–0.5 \AA s^{-1} . The active area of the device was 0.04 cm².

Materials and Film Characterization: UV–vis absorption spectra of the solutions and films were recorded on a UV–vis spectrophotometer (Cary 5000, Agilent Technologies) at wavelengths ranging from 200 to 800 nm. For the absorption of the Sb_2S_3 thin films, TiO_2 -coated FTO glass substrate was used as a background. Raman spectra were acquired using a Renishaw inVia Raman microscope at an excitation laser wavelength of 532 nm with a 100 \times objective. XRD patterns were scanned on a Bruker D8 ADVANCE diffractometer with Cu K α radiation ($\lambda = 1.5418 \text{ \AA}$). XPS data were obtained using a Kratos Axis ULTRA X-ray photoelectron spectrometer incorporating a 165 mm hemispherical electron energy analyzer. The incident radiation was monochromatic Al K α X-rays (1486.6 eV) at 225 W (15 kV, 15 mA). Survey scans were scanned at binding energies between 1200 and 0 eV with an interval of 1.0 eV, while high-resolution scans were conducted with 0.05 eV steps. XPS spectra were fitted using a CASAXPS software. TEM images, EDX elemental mapping, and spectrum were acquired using an FEI Titan Themis. The STEM probe was aberration-corrected, enabling sub-Ångstrom spatial resolution, and HAADF images were obtained. SEM images of the films and devices were collected on a field-emission-scanning electron microscope (JOEL JSM-7001) and a JEOL JSM-7500FA with an accelerating voltage of 5.0 kV. AFM images were collected on a Bruker Dimension Icon atomic

force microscope using a PFTUNA probe operating in ScanAsyst mode and were analyzed using Bruker Nanoscope Analysis.

Device Characterization: The photocurrent density–voltage (J – V) characteristics were analyzed in air using a computerized Keithley 2600 SourceMeter under a simulated one sun (AM1.5G) with an intensity of 100 mW cm^{-2} . A xenon-lamp-based solar simulator (Newport Oriol Solar 3A) was used to evaluate the PV performance of the devices. The light illumination intensity was determined using a standard silicon cell, which was certified by a National Renewable Energy Laboratory. The J – V measurements were performed in both reverse (0.8 to -0.1 V) and forward (-0.1 to 0.8 V) scan directions. The active area of the device was 0.04 cm^2 , and a nonreflective aperture mask was used for device testing. The scan rates ranging from 50 to 600 mV s^{-1} were used to study the effect of scan rates on the PV performances. The EQE spectrum was measured by a light source (a xenon lamp) coupled with a monochromator. The light intensity of the illumination source was adjusted using a photodiode detector (silicon calibrated detector, Newport) with nonreflective mask. The scan was taken within the range of 300–800 nm at intervals of 10 nm. EQE data were collected on a TracQ Basic Software.

The stability of the devices underwater was tested by dipping them in water for 0, 1, and 25 min. No encapsulation was applied to the devices. The photostability of the devices was tested by exposing cells to continuous light illumination (1 sun, xenon lamp) in air. The data were obtained in the reverse scan direction every 10 min over 3 h. The cell stability at a temperature of $85 \text{ }^\circ\text{C}$ (on a hotplate) was also carried out in ambient conditions and tested every 10 min for a total of 1 h using the reverse scan direction.

Statistical Analysis: The average PV parameters and standard deviations shown in Table 1 were calculated based on at least six individual cells. A histogram, illustrated in Figure 5c, showing the PCE distribution was populated based on a total of 22 individual devices.

For stability tests, no preconditioning was applied to the devices prior to testing. EQE spectra (Figure 5d and S13, Supporting Information) were presented with normalized values. The recorded data were normalized based on the highest EQE peaks. The heights of the flakes in Figure S4, Supporting Information, (AFM images) were measured using the line profile tool of Bruker Nanoscope Analysis.

Supporting Information

Supporting Information is available from the Wiley Online Library or from the author.

Acknowledgements

The first authors, M. B.-E. and P.M., are supervised by M.B. M.B.-E. and P.M. contributed equally to this work. This work was financially supported by the Australian Research Council (grant nos. DP190100120, DP200101217, FT200100015, and DE220100521). M.B. acknowledges the support of Griffith University internal grants. A.S.R.B. acknowledges the support from King Abdullah University of Science and Technology (KAUST) through the Ibn Rushd Postdoctoral Fellowship Award and the Australian Government through the Australian Renewable Energy Agency (ARENA), Australian Centre for Advanced Photovoltaics (ACAP). The authors thank Dr. Ashley Slattery of Adelaide Microscopy at the University of Adelaide for his help with TEM analysis. This work was performed in part at the Queensland node of the Australian National Fabrication Facility, a company established under the National Collaborative Research Infrastructure Strategy to provide nano- and micro-fabrication facilities for Australia's researchers. The authors gratefully acknowledge the use of Centre for Microscopy and Microanalysis (CMM) facilities at the University of Queensland, Australia.

Open access publishing facilitated by The University of Queensland, as part of the Wiley - The University of Queensland agreement via the Council of Australian University Librarians.

Conflict of Interest

The authors declare no conflict of interest.

Data Availability Statement

The data that support the findings of this study are available from the corresponding author upon reasonable request.

Keywords

2D materials, antimonene, light-harvesting materials, photovoltaics, Sb_2S_3

Received: March 3, 2022

Revised: March 22, 2022

Published online: April 5, 2022

- [1] Y. Zhu, S. Murali, W. Cai, X. Li, J. W. Suk, J. R. Potts, R. S. Ruoff, *Adv. Mater.* **2010**, *22*, 3906.
- [2] K. S. Novoselov, A. K. Geim, S. V. Morozov, D. Jiang, Y. Zhang, S. V. Dubonos, I. V. Grigorieva, A. A. Firsov, *Science*. **2004**, *306*, 666.
- [3] M. Xu, T. Liang, M. Shi, H. Chen, *Chem. Rev.* **2013**, *113*, 3766.
- [4] N. Rohaizad, C. C. Mayorga-Martinez, M. Fojtů, N. M. Latiff, M. Pumera, *Chem. Soc. Rev.* **2021**, *50*, 619.
- [5] C. Tan, X. Cao, X.-J. Wu, Q. He, J. Yang, X. Zhang, J. Chen, W. Zhao, S. Han, G.-H. Nam, M. Sindoro, H. Zhang, *Chem. Rev.* **2017**, *117*, 6225.
- [6] S. Balendhran, S. Walia, H. Nili, S. Sriram, M. Bhaskaran, *Small* **2015**, *11*, 640.
- [7] X. Kong, Q. Liu, C. Zhang, Z. Peng, Q. Chen *Chem. Soc. Rev.* **2017**, *46*, 2127.
- [8] P. Ares, J. J. Palacios, G. Abellán, J. Gómez-Herrero, F. Zamora, *Adv. Mater.* **2018**, *30*, 1703771.
- [9] X. Wang, X. Yu, J. Song, W. Huang, Y. Xiang, X. Dai, H. Zhang, *Chem. Eng. J.* **2021**, *406*, 126876.
- [10] Y. Wang, Y. Ding, *Phys. Chem. Chem. Phys.* **2015**, *17*, 27769.
- [11] S. Zhang, M. Xie, F. Li, Z. Yan, Y. Li, E. Kan, W. Liu, Z. Chen, H. Zeng, *Angew. Chem. Int. Ed.* **2016**, *55*, 1666.
- [12] S. Zhang, Z. Yan, Y. Li, Z. Chen, H. Zeng, *Angew. Chem. Int. Ed.* **2015**, *54*, 3112.
- [13] P. Ares, F. Aguilar-Galindo, D. Rodríguez-San-Miguel, D. A. Aldave, S. Díaz-Tendero, M. Alcamí, F. Martín, J. Gómez-Herrero, F. Zamora, *Adv. Mater.* **2016**, *28*, 6332.
- [14] C. Gibaja, D. Rodríguez-San-Miguel, P. Ares, J. Gómez-Herrero, M. Varela, R. Gillen, J. Maultzsch, F. Hauke, A. Hirsch, G. Abellán, F. Zamora, *Angew. Chem. Int. Ed.* **2016**, *55*, 14345.
- [15] C. Gibaja, M. Assebban, I. Torres, M. Fickert, R. Sanchis-Gual, I. Brotons, W. S. Paz, J. J. Palacios, E. G. Michel, G. Abellán, F. Zamora, *J. Mater. Chem. A* **2019**, *7*, 22475.
- [16] Q. Xiao, C.-X. Hu, H.-R. Wu, Y.-Y. Ren, X.-Y. Li, Q.-Q. Yang, G.-H. Dun, Z.-P. Huang, Y. Peng, F. Yan, Q. Wang, H.-L. Zhang, *Nanoscale Horiz.* **2020**, *5*, 124.
- [17] W. Tian, S. Zhang, C. Huo, D. Zhu, Q. Li, L. Wang, X. Ren, L. Xie, S. Guo, P. K. Chu, H. Zeng, K. Huo, *ACS Nano* **2018**, *12*, 1887.
- [18] X. Sun, Z. Song, S. Liu, Y. Wang, Y. Li, W. Wang, J. Lu, *ACS Appl. Mater. Interfaces* **2018**, *10*, 22363.
- [19] S. Zhang, W. Zhou, Y. Ma, J. Ji, B. Cai, S. A. Yang, Z. Zhu, Z. Chen, H. Zeng, *Nano Lett.* **2017**, *17*, 3434.

- [20] F. Zhang, J. He, Y. Xiang, K. Zheng, B. Xue, S. Ye, X. Peng, Y. Hao, J. Lian, P. Zeng, J. Qu, J. Song, *Adv. Mater.* **2018**, *30*, 1803244.
- [21] X. Wang, J. He, B. Zhou, Y. Zhang, J. Wu, R. Hu, L. Liu, J. Song, J. Qu, *Angew. Chem. Int. Ed.* **2018**, *57*, 8668.
- [22] Z. Wang, R. Zhang, M. Zhao, Z. Wang, B. Wei, X. Zhang, S. Feng, H. Cao, P. Liu, Y. Hao, H. Wang, B. Xu, S. J. Pennycook, J. Guo, *J. Mater. Chem. A* **2018**, *6*, 23773.
- [23] M. Bat-Erdene, G. Xu, M. Batmunkh, A. S. R. Bati, J. J. White, M. J. Nine, D. Losic, Y. Chen, Y. Wang, T. Ma, J. G. Shapter, *J. Mater. Chem. A* **2020**, *8*, 4735.
- [24] C. C. Mayorga-Martinez, R. Gusmão, Z. Sofer, M. Pumera, *Angew. Chem. Int. Ed.* **2019**, *58*, 134.
- [25] Y. Gao, W. Tian, C. Huo, K. Zhang, S. Guo, S. Zhang, X. Song, L. Jiang, K. Huo, H. Zeng, *J. Mater. Chem. A* **2019**, *7*, 3238.
- [26] J. Ji, X. Song, J. Liu, Z. Yan, C. Huo, S. Zhang, M. Su, L. Liao, W. Wang, Z. Ni, Y. Hao, H. Zeng, *Nat Commun.* **2016**, *7*, 13352.
- [27] G. H. Major, N. Fairley, P. M. A. Sherwood, M. R. Linford, J. Terry, V. Fernandez, K. Artyushkova, *J. Vac. Sci. Technol. A* **2020**, *38*, 061203.
- [28] R. Gusmão, Z. Sofer, D. Bouša, M. Pumera, *Angew. Chem. Int. Ed.* **2017**, *56*, 14417.
- [29] I.-Y. Jeon, H.-J. Choi, S.-M. Jung, J.-M. Seo, M.-J. Kim, L. Dai, J.-B. Baek, *J. Am. Chem. Soc.* **2013**, *135*, 1386.
- [30] R. Kondrotas, C. Chen, J. Tang, *Joule* **2018**, *2*, 857.
- [31] E. Zimmermann, T. Pfadler, J. Kalb, J. A. Dorman, D. Sommer, G. Hahn, J. Weickert, L. Schmidt-Mende, *Adv. Sci.* **2015**, *2*, 1500059.
- [32] Z. Cai, C.-M. Dai, S. Chen, *Solar RRL* **2020**, *4*, 1900503.
- [33] Q. Zhang, B. Kan, X. Wan, H. Zhang, F. Liu, M. Li, X. Yang, Y. Wang, W. Ni, T. P. Russell, Y. Shen, Y. Chen, *J. Mater. Chem. A* **2015**, *3*, 22274.
- [34] A. Ahmed, K. Riaz, H. Mehmood, T. Tauqeer, Z. Ahmad, *Opt. Mater.* **2020**, *105*, 109897.
- [35] S. A. Moiz, A. N. M. Alahmadi, *Polymers* **2021**, *13*, 2110.
- [36] N. K. Elumalai, A. Uddin, *Energy Environ. Sci.* **2016**, *9*, 391.
- [37] S. V. Spataru, D. Sera, P. Hacke, T. Kerekes, R. Teodorescu, *Prog. Photovoltaics Res. Appl.* **2016**, *24*, 517.
- [38] J. A. Christians, J. S. Manser, P. V. Kamat, *J. Phys. Chem. Lett.* **2015**, *6*, 852.
- [39] Y. Wang, X. Liu, Z. Zhou, P. Ru, H. Chen, X. Yang, L. Han, *Adv. Mater.* **2019**, *31*, 1803231.
- [40] G. Tumen-Ulzii, T. Matsushima, D. Klotz, M. R. Leyden, P. Wang, C. Qin, J.-W. Lee, S.-J. Lee, Y. Yang, C. Adachi, *Commun Mater.* **2020**, *1*, 31.
- [41] P. Myagmarsereejid, M. Ingram, M. Batmunkh, Y. L. Zhong, *Small* **2021**, *17*, 2100241.
- [42] M. Batmunkh, T. J. Macdonald, C. J. Shearer, M. Bat-Erdene, Y. Wang, M. J. Biggs, I. P. Parkin, T. Nann, J. G. Shapter, *Adv. Sci.* **2017**, *4*, 1600504.
- [43] J. A. Röhr, J. Lipton, J. Kong, S. A. Maclean, A. D. Taylor, *Joule* **2020**, *4*, 840.
- [44] P. K. Enaganti, S. Soman, S. S. Devan, S. C. Pradhan, A. K. Srivastava, J. M. Pearce, S. Goel, *Prog. Photovoltaics Res. Appl.* **2022**, *215*, 1424.
- [45] L. Shi, M. P. Bucknall, T. L. Young, M. Zhang, L. Hu, J. Bing, D. S. Lee, J. Kim, T. Wu, N. Takamure, D. R. McKenzie, S. Huang, M. A. Green, A. W. Y. Ho-Baillie, *Science* **2020**, *368*, eaba2412.
- [46] A. S. R. Bati, A. A. Sutanto, M. Hao, M. Batmunkh, Y. Yamauchi, L. Wang, Y. Wang, M. K. Nazeeruddin, J. G. Shapter, *Cell Rep. Phys. Sci.* **2021**, *2*, 100598.
- [47] C. Jiang, R. Tang, X. Wang, H. Ju, G. Chen, T. Chen, *Sol. RRL* **2019**, *3*, 1800272.
- [48] M. Bat-Erdene, M. Batmunkh, C. J. Shearer, S. A. Tawfik, M. J. Ford, L. Yu, A. J. Sibley, A. D. Slattery, J. S. Quinton, C. T. Gibson, J. G. Shapter, *Small Methods* **2017**, *1*, 1700260.